nature biotechnology

Molecular afterglow imaging with bright, biodegradable polymer nanoparticles

Qingqing Miao[1], Chen Xie[1], Xu Zhen[1], Yan Lyu[1], Hongwei Duan[1], Xiaogang Liu[2], Jesse V Jokerst[3] & Kanyi Pu[1]

Afterglow optical agents, which emit light long after cessation of excitation, hold promise for ultrasensitive *in vivo* imaging because they eliminate tissue autofluorescence. However, afterglow imaging has been limited by its reliance on inorganic nanoparticles with relatively low brightness and short-near-infrared (NIR) emission. Here we present semiconducting polymer nanoparticles (SPNs) <40 nm in diameter that store photon energy via chemical defects and emit long-NIR afterglow luminescence at 780 nm with a half-life of ~6 min. *In vivo*, the afterglow intensity of SPNs is more than 100-fold brighter than that of inorganic afterglow agents, and the signal is detectable through the body of a live mouse. High-contrast lymph node and tumor imaging in living mice is demonstrated with a signal-to-background ratio up to 127-times higher than that obtained by NIR fluorescence imaging. Moreover, we developed an afterglow probe, activated only in the presence of biothiols, for early detection of drug-induced hepatotoxicity in living mice.

Optical imaging plays a crucial role in biology and medicine[1]; however, the need for real-time light excitation during imaging produces tissue autofluorescence, which compromises imaging sensitivity and specificity in living subjects[2]. Therefore, optical imaging strategies such as bioluminescence and Cerenkov luminescence that eliminate the need for concurrent light excitation have attracted tremendous interest[3,4]. However, bioluminescence probes require enzyme and substrate to produce light emission, and thus their signals are often affected by enzyme microenvironment and substrate biodistribution in living animals[5]. By contrast, Cerenkov probes rely on toxic ionizing radiation and release of charged particles from radioisotopes; this drawback is further compounded by their intrinsic blue light emission with shallow tissue penetration[6].

Afterglow luminescence is an intrinsic luminescent process that occurs after the end of light excitation[7]. Afterglow luminescence is generally caused by the slow release of photons from energy traps in the materials upon thermal stimulation. Although afterglow imaging has tremendous promise for *in vivo* imaging because of the lack of real-time excitation, only a few inorganic nanoparticles have been shown to produce afterglow in biologically relevant conditions[8–11], and all of these contain rare-earth heavy metal ions such as europium, praseodymium and chromium (**Supplementary Table 1**)[12–17]. Thus, the current generation of afterglow probes are potentially hampered owing to toxicity concerns[18].

Furthermore, inorganic afterglow nanoparticles have limited targeting ability because their surface is difficult to modify; they are currently used as accumulation probes[7–9,19,20]. Thus, contrast is determined by the difference in probe concentration between target tissue and adjacent normal tissue. Smart activatable probes that undergo a change in signal intensity upon detecting molecular targets, on the other hand, offer high contrast and real-time information on pathological conditions at the molecular level[21,22]. To date, however, the benefits of afterglow imaging and activatable probes have rarely been explored for *in vivo* imaging[23].

In this study, we report the design and application of SPNs as biodegradable afterglow luminescence probes for molecular imaging in living mice. SPNs are built from optically active semiconducting polymers (SPs) and are a class of photonic nanomaterials[24]. They are completely organic and contain biologically benign ingredients to avoid metal-ion-induced toxicity[25]. Due to their structural flexibility and excellent optical properties, SPNs can be used as fluorescence, chemiluminescence, bioluminescence or photoacoustic agents for a variety of *in vivo* applications including tumor imaging[26], neuroinflammation imaging[27], lymph node mapping[28], ultrafast hemodynamic imaging[29] and neuron activation[30,31]. Although we recently observed the afterglow phenomenon in an SPN, its mechanism and *in vivo* utility remain unexplored[32].

In the following, we first investigate the mechanism of SPN afterglow luminescence and find that it involves light-induced formation of unstable chemical defects that can produce photons as downstream products. We then propose a strategy to effectively amplify and redshift the afterglow of SPNs and use it for lymph node and tumor imaging in living mice. Finally, we demonstrate the feasibility of developing SPNs into activatable afterglow molecular probes for *in vivo* monitoring of drug-induced hepatotoxicity.

RESULTS

Screening of SPs for afterglow

SPs with different molecular structures were tested to identify structures capable of afterglow luminescence (**Fig. 1a**). Nanoprecipitation was used to transform seven SPs into water-soluble nanoparticles in the presence of an amphiphilic triblock copolymer (PEG-*b*-PPG-*b*-PEG) (**Fig. 1b**). The hydrodynamic diameters of the SPNs measured by dynamic light scattering were similar, ranging from

[1]School of Chemical and Biomedical Engineering, Nanyang Technological University, Singapore. [2]Department of Chemistry, National University of Singapore, Singapore. [3]Department of NanoEngineering, University of California San Diego, La Jolla, California, USA. Correspondence should be addressed to: K.P. (kypu@ntu.edu.sg).

Received 11 February; accepted 14 September; published online 16 October 2017; doi:10.1038/nbt.3987

30 to 40 nm (**Fig. 1c**). Transmission electron microscopy (TEM) further confirmed the spherical morphology with an average diameter of 33.9 ± 4.3 nm (**Fig. 1d**), which was nearly identical to the dynamic light scattering data. The nanoparticle solutions were translucent (**Fig. 1e**) with no precipitates or size changes even after 2 months of storage (**Supplementary Fig. 1**), suggesting excellent stability in aqueous solution.

The fluorescence and afterglow signals of SPNs were collected with the IVIS Spectrum imaging system under fluorescence (with excitation) and bioluminescence (without excitation) modes, respectively. Only phenylenevinylene (PPV)-based SPNs including BOPPV, MDMOPPV and MEHPPV showed obvious afterglow luminescence (**Fig. 1e**,**h**); their luminescence spectral profiles were similar to the fluorescence spectra (**Fig. 1f**,**g**). However, all SPNs were highly fluorescent (**Fig. 1e**,**f**). The fluorescence of SPN-MEHPP was undetectable because its absorption wavelength is too short to be excited by the IVIS Spectrum imaging system (**Supplementary Fig. 2**).

That afterglow signal was seen only in PPV-based SPs suggests that phenylenevinylene plays an essential role in the production of luminescence. However, some PPV-based SPs including SPN-MEHCPV and SPN-POPPV did not emit detectable afterglow luminescence. This implies that the substituents on the PPV backbone were also relevant. Similar afterglow behaviors were observed for SPs dispersed in tetrahydrofuran (THF) (**Supplementary Fig. 3**). This confirms that the chemical structure rather than the nanoparticle structure of an SP controls SPN afterglow. Moreover, the afterglow of SPNs was independent of their sizes (**Supplementary Fig. 4**).

Mechanistic study of afterglow

To identify the underlying mechanism governing SPN afterglow luminescence, we studied the effect of light irradiation on the chemical structures of SPs. The absorption peak of MEHPPV at 493 nm showed a strong hypochromatic shift and an intensity decrease after irradiation, indicating a breakdown in the conjugation length and thus the decomposition of MEHPPV (**Fig. 2a**). Proton nuclear magnetic resonance (^{1}H NMR) analysis showed two new peaks at 9.88 and 10.47 p.p.m. after light irradiation (**Fig. 2b**). These were assigned to the aldehyde and carboxyl peaks, respectively. Peak broadening and division are caused by different chemical environments and indicate the formation of inhomogeneous fragments. The characteristic peaks of oxidized MEHPPV fragments were also detected in Fourier transform infrared spectroscopy (FTIR) at 1,728 cm^{-1}. In addition, the peak at 3,053 cm^{-1} corresponding to ethene-1,2-diyl groups was attenuated after light irradiation, further proving the oxidation of vinylene bonds (**Fig. 2c**). Similar spectral changes were also observed for BOPPV and MDMOPPV (**Supplementary Fig. 5**), but other SPs didn't show obvious changes (**Supplementary Fig. 6**). Thus, these data clearly suggest that light irradiation oxidizes vinylene bonds in some PPVs to break them into inhomogeneously oxidized fragments.

Next, a singlet oxygen sensor green (SOSG) was applied to test for the generation of singlet oxygen ($^1O_2$) during light-induced oxidation. After light irradiation of the SPN-MEHPPV solution for 5 min, the fluorescence intensities of SOSG at 528 nm increased by 1.69-fold (**Fig. 2d**). This proved that $^1O_2$ was produced during irradiation and was responsible for the oxidization of MEHPPV. Based on this observation, we propose a mechanism of afterglow luminescence of PPV-based SPNs (**Fig. 2g**). Light irradiation of PPVs generates $^1O_2$ that oxidizes the vinylene bond (C = C) via π^2-π^2 cycloaddition to form a PPV-dioxetane intermediate. This intermediate is unstable[33] and can spontaneously degrade into a PPV-aldehyde and generate photons. Further oxidation of the PPV-aldehyde yields PPV-carboxyl as the final product of the light-irradiation reaction. Thus, the key step in afterglow luminescence is $^1O_2$-induced formation of PPV-dioxetane, which is determined by the oxidative sensitivity of the vinyl bond in PPVs. This explains why not all PPV-based SPNs had afterglow, as well as the role of the substituent. In fact, only PPVs with electron-donating substituents (alkoxyl groups), including BOPPV, MDMOPPV and MEHPPV, showed detectable afterglow luminescence. Other derivatives with weak electron-donating (alkyl groups for POPPV) or strong electron-withdrawing substituents (cyano groups for MEHCPV) did not.

The afterglow luminescence of PPV-based SPNs is long lasting with a half-life of 6.6 min at biologically relevant conditions (pH = 7.4 at 37 °C; **Fig. 2e**). The afterglow conditions can be controlled by changing the reaction conditions including temperature and oxygen levels as well as the addition of an $^1O_2$ scavenger. By intervention in the first pre-light-irradiation step (**Fig. 2f**), the afterglow of SPN-MEHPPV could be increased by 1.25-fold or decreased by 2.82-fold when measured in O_2- and N_2-saturated solutions, respectively. Moreover, the addition of the $^1O_2$ scavenger (NaN_3) could reduce the afterglow intensity by 2.06-fold. By intervention in the second decomposition step (**Fig. 2f**), the afterglow intensity could be increased fivefold by elevating the temperature from 37 to 60 °C. It was nearly completely inhibited at 0 °C (**Supplementary Fig. 7**). Such a temperature-dependent afterglow could be useful for real-time monitoring of temperature during photothermal therapy (**Supplementary Fig. 8**). Similar afterglow behaviors were observed for SPN-MDMOPPV and SPN-BOPPV (**Supplementary Fig. 7**). Taken together, these data not only further validate the proposed mechanism of afterglow but also highlight the important role of the $^1O_2$ species in determining the afterglow brightness of SPNs.

Optimization of afterglow

The NIR light ranging from 700 to 2,500 nm penetrates biological tissues more efficiently than visible light due to reduced tissue scattering and minimized biological autofluorescence in this region[2]. To amplify afterglow and red-shift it into the ideal NIR optical imaging window, a $^1O_2$ sensitizer, silicon 2,3-naphthalocyanine bis(trihexylsilyloxide) (NCBS), was doped into SPN-MEHPPV via nanoprecipitation (**Fig. 3a**). Because NCBS can absorb in the NIR region (**Supplementary Fig. 9a**), it induces afterglow by pre-irradiation at 808 nm. Thus, SPNs with different weight percentages of NCBS (1, 2.5, 5 and 10% w/w) were prepared and defined as SPN-NCBS1, SPN-NCBS2.5, SPN-NCBS5 and SPN-NCBS10, respectively. Doping had no obvious effect on the size and morphology of the SPNs (**Supplementary Fig. 10**). The MEHPPV fluorescence at 580 nm gradually decreased with increasing doping concentration along with a gradual increase in NCBS emission at 775 nm (**Fig. 3d** and **Supplementary Fig. 11**). This spectral change confirmed the efficient energy transfer from MEHPPV to NCBS. Saturation occurred at 5%—further increases in doping concentration decreased the emission of NCBS (**Supplementary Fig. 11**), owing to the self-quenching of NCBS at elevated local concentrations within the nanoparticles.

Regardless of the pre-irradiation laser wavelength (808 or 514 nm), the afterglow intensities at both 580 and 775 nm increased with increasing doping concentration (**Fig. 3c**,**e**,**f**). The laser irradiation conditions were optimized (**Supplementary Fig. 12**). Signal quantification showed that the absolute afterglow intensities induced by pre-irradiation at 514 nm increased by 6.8-fold when comparing the optimal SPN (SPN-NCBS5) with the non-doped control SPN (SPN-MEHPPV) (**Fig. 3f**). Moreover, the afterglow of SPN-NCBS5 could be further enhanced by 11-fold at 808 nm versus 514 nm at the same

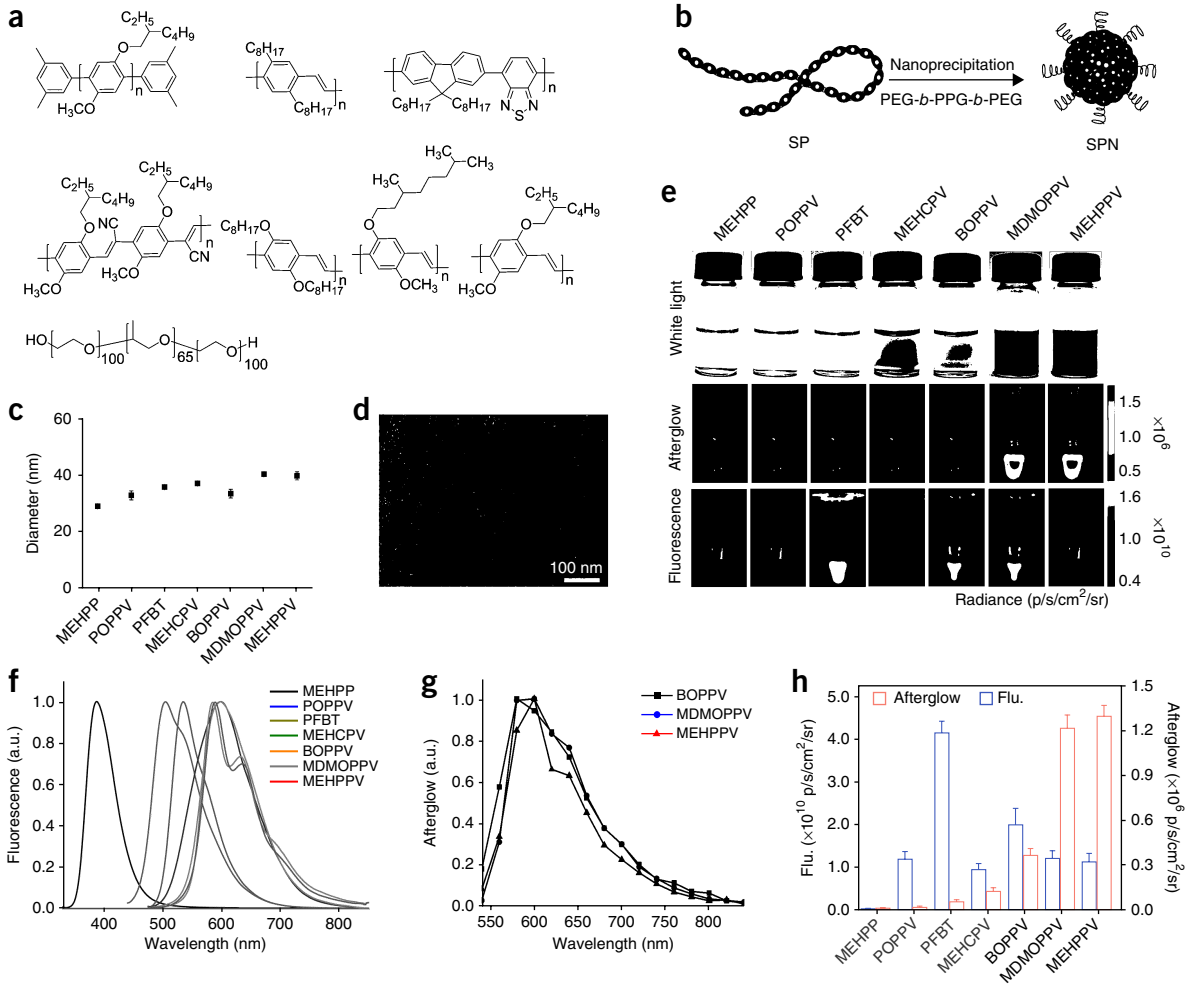

Figure 1 Synthesis and characterization of SPNs. (**a**) Chemical structures of the SPs (MEHPP, POPPV, PFBT, MEHCPV, BOPPV, MDMOPPV and MEHPPV) and the amphiphilic triblock copolymer (PEG-*b*-PPG-*b*-PEG) used for the synthesis of SPNs. (**b**) Schematic illustration of the preparation of SPNs through nanoprecipitation. (**c**) Average hydrodynamic diameters of SPNs in 1× PBS buffer (pH = 7.4). (**d**) Representative TEM image of SPN-MEHPPV. (**e**) White-light (up panel), afterglow luminescence (middle panel) and fluorescence (bottom panel) images of SPN-MEHPP, SPN-POPPV, SPN-PFBT, SPN-MEHCPV, SPN-BOPPV, SPN-MDMOPPV and SPN-MEHPPV in 1× PBS buffer (pH = 7.4). The fluorescence and afterglow images of SPNs were taken at the same absorption intensities at their respective maximum (the absorption is 0.5 after tenfold dilution of the solution). The fluorescence images were acquired upon excitation at 465 nm for all SPNs except for SPN-MEHPP and SPN-POPPV (430 nm). The afterglow images were acquired for 30 s after the pre-irradiation of SPNs under white light at a power density of 0.1 W/cm^2 for 1 min. (**f**) Normalized fluorescence spectra of SPNs in 1 × PBS buffer (pH = 7.4). (**g**) Normalized afterglow luminescence spectra of SPN-BOPPV, SPN-MDMOPPV and SPN-MEHPPV in 1× PBS buffer (pH = 7.4). (**h**) Quantification of fluorescence and afterglow intensities of SPNs in **e**. The error bars represent the s.d. (n = 3).

power density (**Fig. 3b**,**c**,**f**). This was attributed to NCBS's stronger ability to generate $^1O_2$ relative to MEHPPV (**Supplementary Fig. 13**). No afterglow was detected for the nanoparticles composed of NCBS5 only (**Supplementary Fig. 11c**). The $^1O_2$ sensitizer-amplified afterglow was also observed for (TPP)-meso-tetraphenylporphyrin doped SPN-MEHPPV and NCBS- or TPP-doped SPN-MDMOPPV (**Supplementary Figs. 14** and **15**). These data suggest that $^1O_2$ sensitizers are intraparticle promoters to effectively amplify the afterglow of SPNs and modulate their emission wavelengths.

Tissue penetration study of afterglow

The suitability of the amplified afterglow nanoparticle (SPN-NCBS5) for biological applications was first verified by the good cytocompatibility (**Supplementary Fig. 16**) size and, optical stability (**Supplementary Figs. 17** and **18**) and biodegradability of SPN-NCBS5 (**Supplementary Fig. 19**). The penetration depth and imaging sensitivity for the afterglow of SPN-NCBS5 were then examined both *in vitro* and *in vivo*. Because the SPN-NCBS5 had absorption and emission in the NIR region (**Supplementary Figs. 9** and **11**), the fluorescence was acquired at 780 nm upon excitation at 710 nm (**Supplementary Fig. 9b** shows the spectrum); the afterglow was induced by pre-irradiation at 808 nm.

Next, increasingly thick pieces of chicken tissue were placed on top of the samples, and the signals for both afterglow and fluorescence decreased (**Fig. 4a**,**b**). Due to the low background noise for afterglow (824 ± 109 p/s/cm^2/sr) versus fluorescence (2.53 × 10^7 ± 1.76 × 10^6 p/s/cm^2/sr), the signal to background ratio (SBR) for afterglow (291 ± 18) was 67 times higher than that for fluorescence (4.33 ± 0.96) at a thickness of 1.5 cm. Moreover, the NIR fluorescence was close to the background noise at the thickness of 4 cm, whereas the SBR for afterglow was still 17.7 ± 0.27. Similarly, the background for afterglow luminescence imaging of a living mouse was as low as 867 ± 80 p/s/cm^2/sr, because tissue autofluorescence was eliminated in the absence of

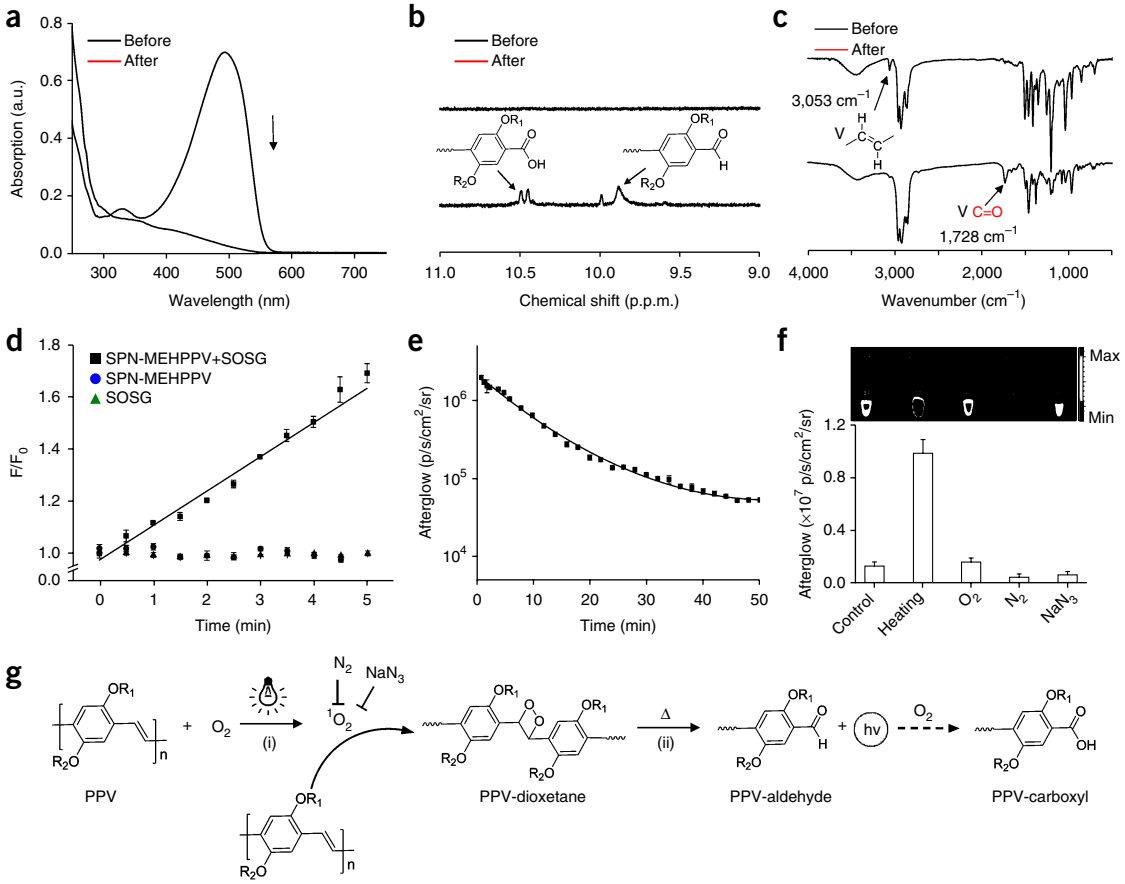

Figure 2 Mechanistic study of the afterglow of SPNs. (**a**) UV-Vis absorption spectra of MEHPPV (10 μg/mL) before and after light irradiation for 4 h in $CHCl_3$ (power: 0.1 W/cm^2). (**b**) ^{1}H NMR spectra of MEHPPV before and after light illumination for 24 h in $CDCl_3$ (power: 0.1 W/cm^2). (**c**) FTIR spectra of MEHPPV before and after light illumination for 24 h in $CHCl_3$ (power: 0.1 W/cm^2). (**d**) Fluorescence enhancement (F/F_0) of SOSG (1 μM) at 528 nm in the absence or presence of SPN-MEHPPV (1.25 μg/mL) as a function of light irradiation time. (**e**) Decay of afterglow luminescence of SPN-MEHPPV (62.5 μg/mL) at room temperature. The nanoparticle solution was pre-illuminated for 1 min under white light at a power density of 0.1 W/cm^2 before the collection of afterglow signals. (**f**) Afterglow images and intensities of SPN-MEHPPV (62.5 μg/mL) acquired at different temperatures (room temperature and 60 °C), after treatment by N_2, O_2 purging or in the presence of 50% w/w NaN_3. (**g**) Proposed mechanism for the afterglow luminescence of PPV-based SP. R_1 and R_2 are alkyl chains. The error bars represent the s.d. ($n = 3$).

real-time excitation. Thus, when detecting the NIR-induced afterglow signals from SPN-NCBS5 at a depth of 1.7 cm through a living mouse (**Fig. 4c–e**), the SBR reached 237 ± 22, which was 4.7 and 120 times higher than the visible-light-induced afterglow (50.7 ± 4.5) and the NIR fluorescence (1.98 ± 0.09), respectively. As decomposition caused by light irradiation was a slow and gradual process, the afterglow could be repeatedly recharged by *in situ* irradiation at 808 nm through chicken tissue or a living mouse (**Supplementary Figs. 20–22**), confirming the feasibility of long-term *in vivo* imaging.

The afterglow signals of SPN-NCBS5 implanted subcutaneously in living mice had a linear correlation with its concentrations (**Supplementary Fig. 23c**). As a result of the high SBR of afterglow, the limit of detection of SPN-NCBS5 in living mice was 1.35 ng/mL (**Supplementary Fig. 23c**)—80 times lower than that for NIR fluorescence (**Supplementary Fig. 23d**). Furthermore, the afterglow of SPN-NCBS5 could be preserved at −20 °C after pre-irradiation, and the intensity dropped by only 3.8% after 1 d of storage (**Supplementary Fig. 24**). This showed the feasibility of using the pre-irradiated afterglow SPNs directly from storage for *in vivo* imaging with no need for any optical pretreatment.

Afterglow imaging of lymph nodes and tumors

The storable and NIR-renewable afterglow of the amplified SPN (SPN-NCBS5) was used for real-time mapping of lymph nodes in living mice (**Fig. 5a**). Lymph node mapping is clinically important in guiding surgical resection of tumor tissues[34], but has not been achieved with afterglow imaging previously. The pre-irradiated SPN-NCBS5 was stored at −20 °C for 1 d, warmed to room temperature, and then directly injected into the forepaw of living mice for continuous imaging without re-irradiation. At t = 30 min post-injection, afterglow and fluorescence images were acquired with an IVIS Spectrum imaging system. The axillary lymph node was clearly delineated with both afterglow and fluorescence imaging (**Supplementary Fig. 25**), indicating an efficient accumulation and retention of SPN-NCBS5 in sentinel lymph nodes. Despite the decay of afterglow over 30 min at 37 °C in living mice (**Supplementary Fig. 26a**), the SBR of afterglow images was still 7.8 ± 1.2, which is twice as high as the fluorescence images (3.9 ± 0.3) (**Fig. 5c**). After the *in situ* renewal of afterglow at t = 65 min post-injection by irradiation at 808 nm for 1 min, the SBR of afterglow image substantially increased to 419 ± 32, 127-fold higher than fluorescence (**Fig. 5b**,**c**). Thus, the NIR afterglow of SPN-NCBS5 could

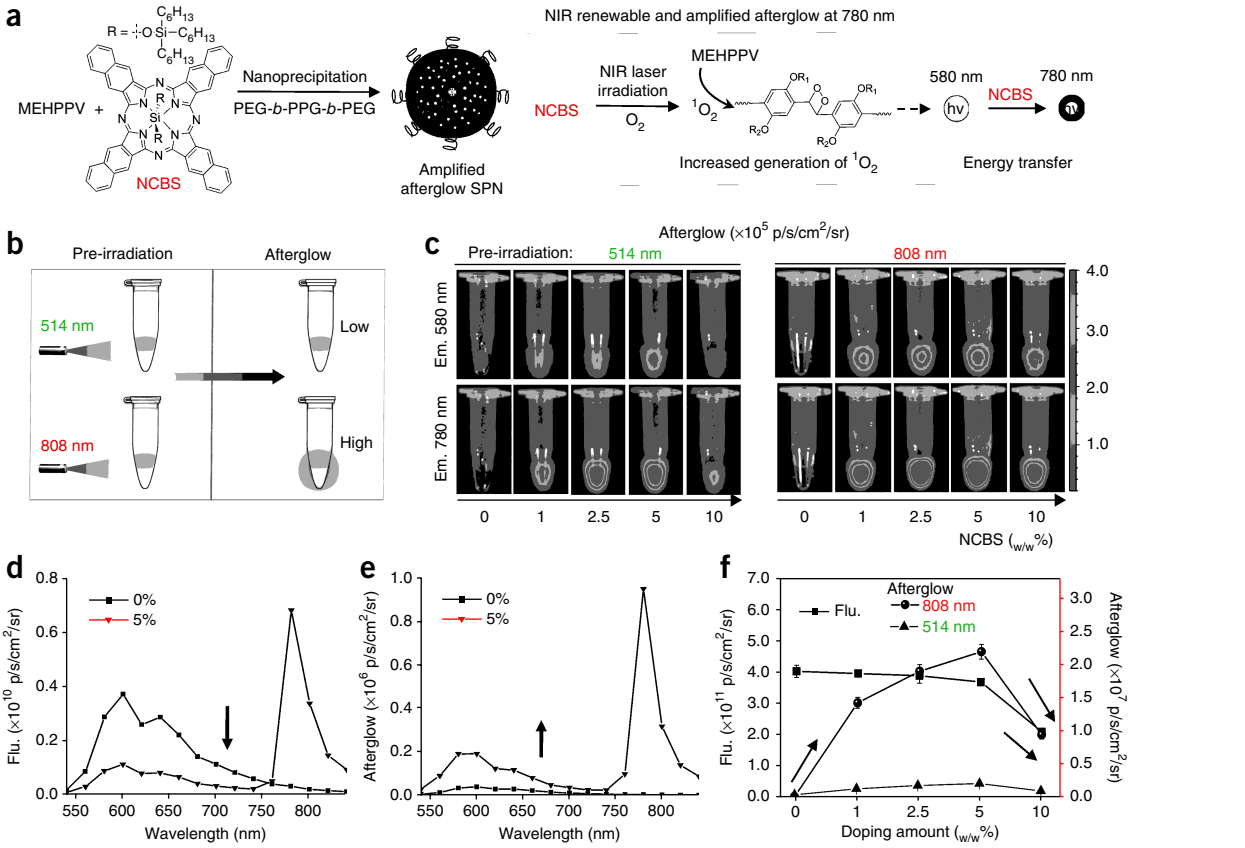

Figure 3 $^1O_2$-sensitizer-amplified NIR afterglow. (**a**) Schematic illustration of the proposed mechanism for $^1O_2$-sensitizer-amplified NIR afterglow. (**b**) Schematic illustration of SPN-NCBS pre-irradiated by an 808-nm laser for afterglow enhancement versus a 514-nm laser. (**c**) Afterglow luminescence images of 12.5 μg/mL SPN-NCBS (based on the mass of MEHPPV) pre-irradiated at 514 (left) or 808 nm (right). The nanoparticle solutions were pre-irradiated by 808- or 514-nm laser (1 W/cm^2) for 1 min, and then the afterglow images were acquired under bioluminescence mode with an acquisition time of 30 s after removal of the laser source. (**d**,**e**) Fluorescence (**d**) and NIR-induced afterglow luminescence spectra (**e**) of SPN-MEHPPV and SPN-NCBS5 in 1× PBS buffer (pH = 7.4). (**f**) Quantification of the absolute fluorescence and afterglow luminescence intensities of SPN-MEHPPV at different doping amounts of NCBS. The error bars represent the s.d. (n = 3).

map the lymph nodes with high contrast and no need for real-time excitation during imaging.

The afterglow luminescence of SPN-NCBS5 was also tested and compared with NIR fluorescence for passively targeted imaging of tumors in living mice. After tail vein injection of SPN-NCBS5, afterglow and NIR fluorescence signals were acquired in real time. Both signals gradually increased over time, but the SBR of afterglow images was higher than that of NIR fluorescence at all time points (**Fig. 5d–f**). Due to the low background of afterglow, the tumor was visible at t = 1 h post-injection and clearly visualized at t = 2 h post-injection for afterglow imaging (**Fig. 5e**); by contrast, the tumor could be visualized only at t = 8 h post-injection with NIR fluorescence imaging. At t = 2 h, the SBR of afterglow images was 149.7 ± 9.0—23.3-fold higher than the NIR fluorescence images (6.4 ± 0.9) (**Fig. 5f**). Both afterglow and fluorescence signals plateaued at t = 36 h post-injection, indicating the efficient accumulation of SPN-NCBS5 in the tumor. The *ex vivo* data further illustrated that SPN-NCBS5 had the highest uptake in liver followed by tumor, lung, and other major organs (**Supplementary Fig. 27**). Thus, the afterglow of SPN-NCBS5 permitted faster and higher contrast imaging of tumors in living mice versus NIR fluorescence imaging.

Afterglow imaging of drug-induced hepatoxicity

Drug-induced hepatotoxicity is a long-standing concern of modern medicine[35]. It is one of the most common reasons that the US Food and Drug Administration withholds drug approval[36]. Evaluation of potential hepatotoxicity in advance of regulatory approval is challenging because currently studies performed *in vitro* often have low predictive power[37]. Oxidative stress and the consumption of antioxidants in the liver are concurrent early events in hepatotoxicity[38]. Biothiols including cysteine (Cys), homocysteine (Hcy) and glutathione (GSH) constitute a major portion of the total body antioxidants that defend against oxidative stress. Thus, real-time *in situ* imaging of biothiol levels can be a feasible way to evaluate drug-induced hepatotoxicity.

To develop activatable afterglow probes for biothiol imaging, we synthesized an amphiphilic oligomer conjugated with an electron-withdrawing quencher (2,4-dinitrophenylsulfonyl, DNBS) and co-precipitated it with NCBS and MEHPPV (**Fig. 6a**). The resulting activatable nanoprobe (SPN-thiol) had a similar size and morphology as other SPNs (**Supplementary Fig. 28**). Due to the efficient electron transfer from the core to the quencher, the afterglow of the SPN-thiol was substantially quenched at its initial afterglow "off" state (**Fig. 6a**). However, in the presence of biothiols including GSH, Cys and Hcy,

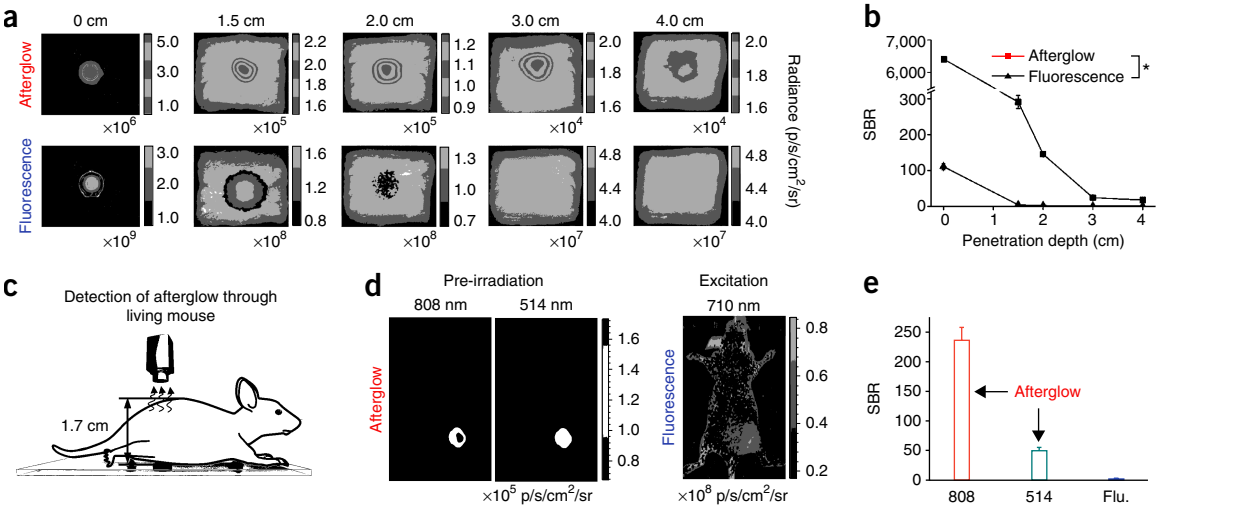

Figure 4 Tissue-penetration study of NIR afterglow luminescence. (**a**) Afterglow luminescence (upper panel) and fluorescence (lower panel) imaging of the SPN-NCBS5 solutions through chicken tissues of different thickness. (**b**) SBRs for afterglow luminescence and fluorescence of SPN-NCBS5 as a function of tissue depth. *Statistically significant difference between fluorescence and afterglow intensities in SBRs through chicken tissues at 4 cm ($n = 3$, unpaired t-test (two-tailed), $t = 95.47$, df = 4, $^*P < 0.0001$). (**c**) Schematic illustration of afterglow luminescence imaging through a living mouse, where the SPN-NCBS5 solutions is located under the mouse with a depth of 1.7 cm. (**d**) Afterglow luminescence and fluorescence images of the SPN-NCBS5 solution through a living mouse. The SPN-NCBS5 solutions (62.5 μg/mL, 50 μL) were pre-irradiated with 808- or 514-nm laser (1 W/cm^2) for 1 min and then the images were collected within 5 s after removing the laser. The fluorescence images were acquired at 780 nm upon excitation at 710 nm. (**e**) SBRs for afterglow luminescence and fluorescence imaging in **d**.

the sulfonamide bond on the surface of SPN-thiol could be cleaved, releasing DNBS from the nanoparticle surface. Thus, the electron transfer was abolished leading to activated afterglow (afterglow "on" state). Upon activation by Cys, the afterglow of SPN-thiol at 780 nm increased by 8.3-fold (**Fig. 6b**). This was 1.75- and 1.41-fold higher than the activation by GSH and Hcy, respectively. By contrast, the

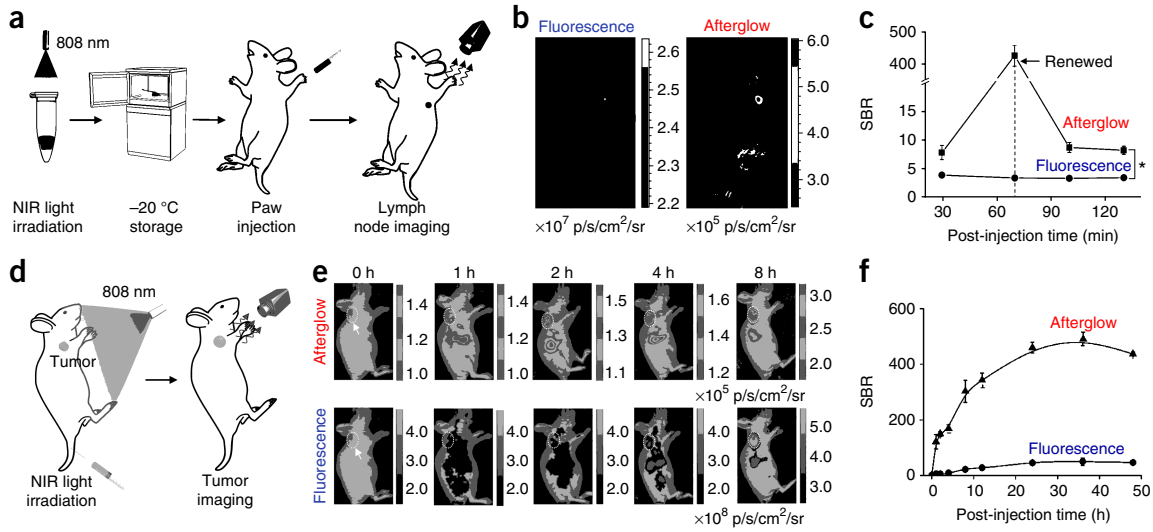

Figure 5 *In vivo* afterglow imaging of lymph nodes and tumor. (**a**) Schematic illustration of afterglow luminescence imaging of a lymph node. SPN-NCBS5 was pre-irradiated with an 808-nm laser (1 W/cm^2) for 1 min followed by storage in –20 °C for 1 d before being directly used for lymph node imaging. (**b**) Fluorescence (left) and afterglow luminescence (right) imaging of a lymph node in a living mouse at $t = 65$ min after intradermal injection of SPN-NCBS5 (0.25 mg/mL, 0.05 mL) into the forepaw of mouse. (**c**) SBRs for afterglow luminescence and fluorescence imaging of a lymph node in living mice as a function of post-injection time. *In situ* renewed afterglow of SPN-NCBS5 was conducted at $t = 65$ min post-injection by irradiation at 808 nm (1 W/cm^2) for 1 min. *Statistically significant difference between fluorescence and afterglow intensities in SBRs at $t = 130$ min after intradermal injection ($n = 3$, unpaired t-test (two-tailed), $t = 11.04$, df = 4, $^*P = 0.004$). (**d**) Schematic illustration of afterglow luminescence imaging of xenograft HeLa tumor in mouse model. (**e**) Afterglow luminescence (upper panel) and fluorescence images (lower panel) of a tumor in a living mouse at representative time points after systemic administration of SPN-NCBS5 (0.25 mg/mL, 0.2 mL) via tail vein injection. The tumor was on the right shoulder as indicated by the white dashed circles and arrows. (**f**) SBRs for afterglow luminescence and NIR fluorescence imaging of a tumor in a living mouse as a function of time. Intensity values are the mean ± s.d. for $n = 3$ mice. Afterglow luminescence images were acquired for 180 s after irradiation at 808 nm (0.5 W/cm^2) for 1 min. The fluorescence images were acquired for 0.1 s at 780 nm upon excitation at 710 nm.

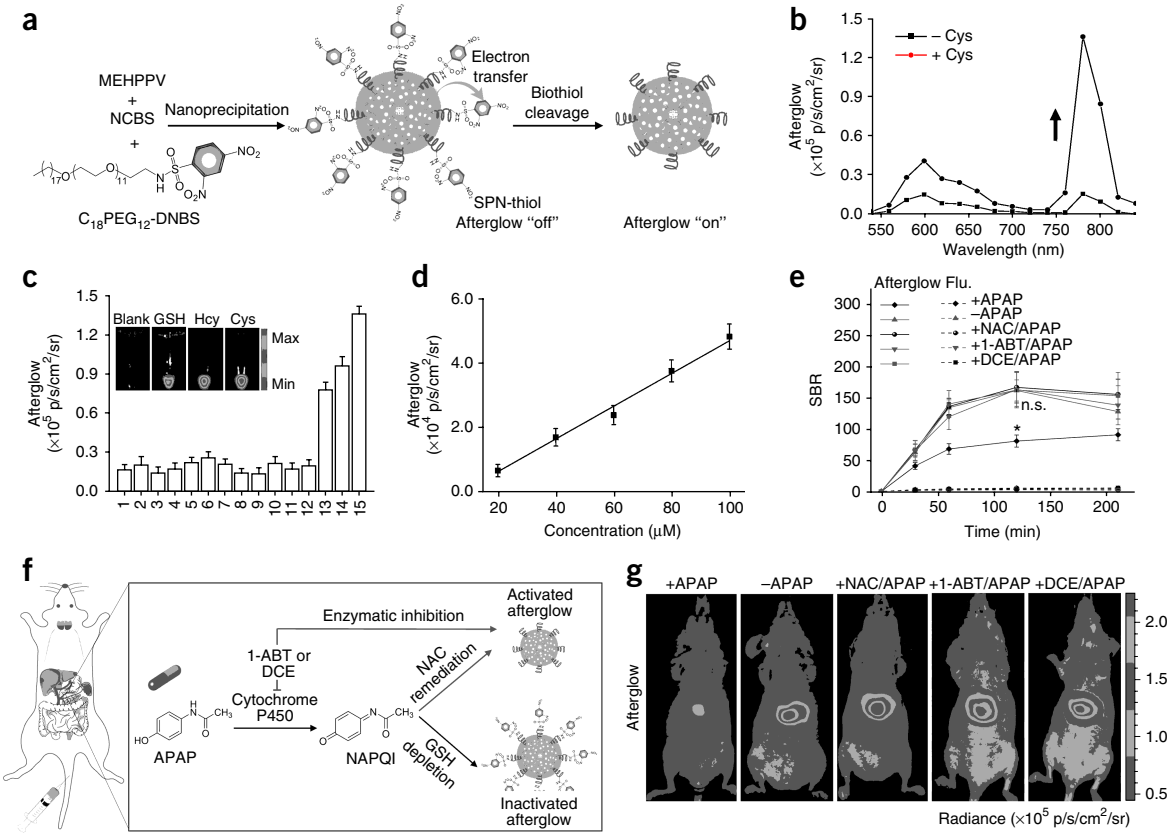

Figure 6 Afterglow luminescence imaging of drug-induced hepatotoxicity. (**a**) Schematic illustration of the design and turn-on mechanism of biothiol-activatable afterglow probe (SPN-thiol). (**b**) Afterglow luminescence spectra of SPN-thiol (12.5 μg/mL) in the absence or presence of Cys (1 mM) in 1× PBS buffer (pH = 7.4). (**c**) Afterglow luminescence intensities of SPN-thiol in the presence of Cys, Hcy, GSH and other amino acids (1 mM) in 1× PBS (pH = 7.4) at 37 °C. 1: Blank, 2: arginine, 3: asparagine, 4: glutamine, 5: glycine, 6: histidine, 7: leucine, 8: lysine, 9: methionine, 10: proline, 11: serine, 12: valine, 13: GSH, 14: Hcy, 15: Cys. Inset: afterglow luminescence imaging of SPN-thiol (12.5 μg/mL) in the absence or presence of GSH, Hcy or Cys (1 mM) in 1 × PBS (pH = 7.4) at 37 °C. (**d**) Fitted calibration curve for the afterglow luminescence intensity of SPN-thiol as a function of the concentration of Cys. (**e**) SBRs for afterglow luminescence and NIR fluorescence imaging of liver in living mice as a function of time. Intensities values are the mean ± s.d. for $n = 3$ mice. *Statistically significant difference in the afterglow luminescence intensities between saline- and APAP-treated groups at $t = 2$ h post-injection of SPN-thiol ($n = 3$, unpaired t-test (two-tailed), $t = 7.183$, df = 4, $^*P = 0.002$); n.s.: no statistically significant differences were seen between saline, NAC/APAP-, 1-ABT/APAP- and DCE/APAP-treated groups at $t = 2$ h post-injection of SPN-thiol ($n = 3$, one-way ANOVA, $P = 0.99$). (**f**) Schematic representation of SPN-thiol for afterglow luminescence imaging of APAP-induced hepatotoxicity. Metabolism of APAP by CYP450 leads to the formation of *N*-acetylparaquinonimine (NAPQI) and causes depletion of GSH, resulting in inactivated afterglow. Utilization of NAC or enzyme inhibitors (DCE or 1-ABT) remediates hepatotoxicity, leading to activated afterglow. (**g**) Representative afterglow luminescence images of mice treated intraperitoneally with APAP (300 mg/kg), saline, NAC (200 mg/kg) with APAP (300 mg/kg), 1-ABT (100 mg/kg) 12 and 24 h before APAP treatment (300 mg/kg) or DCE (0.2 mg/kg) 2 h before APAP treatment (300 mg/kg), followed by an intravenous injection of SPN-thiol (0.25 mg/mL, 0.2 mL) at $t = 20$ min later. Afterglow luminescence images were acquired for 180 s after irradiation at 808 nm (1 W/cm^2) for 1 min.

signals remained nearly undetectable for other amino acids (**Fig. 6c**) as well as for reactive oxygen species (ROS) (**Supplementary Fig. 29**). Thus, SPN-thiol had high selectivity toward biothiols, particularly Cys, and its signal was not interfered with by ROS. Similar activation was observed for the fluorescence of SPN-thiol (**Supplementary Fig. 30**). In addition, a linear correlation between the afterglow intensities and the concentrations of Cys was observed with a limit of detection of 0.60 μM (**Fig. 6d**), which was more than appropriate for *in vivo* biological concentrations of biothiols (~0.1 to 10 mM).

SPN-thiol was used for *in vivo* imaging of drug-induced hepatotoxicity (**Fig. 6f**). Acetaminophen (APAP), an antipyretic analgesic drug, was used as a model drug in view of its well-established hepatotoxicity mechanism. An overdose of APAP can induce oxidative and nitrosative stress and in turn deplete biothiols to initiate a signaling cascade resulting in necrotic cell death. The mice were first treated with APAP at the toxic dosage level or with saline, and then SPN-thiol was systematically administered via intravenous injection at $t = 20$ min post-treatment of APAP. Afterglow and fluorescence signals were acquired in real time, and they gradually increased over time (**Fig. 6e**). At $t = 2$ h post-injection of SPN-thiol, the afterglow of APAP-treated mice was 1.99-times lower than that of saline-treated control mice (**Fig. 6e**,**g**) owing to the decreased level of biothiols in liver. By contrast, when the mice were protected with the antioxidant drug (*N*-acetyl-*L*-cysteine, NAC) or the inhibitors of Cytochrome P450 (CYP450) (trans-1,2-dichloroethylene: DCE and 1-aminobenzotriazole: 1-ABT) before APAP treatment, the afterglow signal was comparable to that for the saline-treated control mice. This was attributed to the ROS scavenging and the inhibition of CYP450-induced drug metabolism for NAC and DCE/1-ABT, respectively. Fluorescence imaging and biodistribution studies showed similar results (**Supplementary Figs. 31** and **32**). Histological studies further showed no histological changes in liver tissue 30 min after APAP

challenge, and massive hepatic necrosis of the livers was only observed 3.5 h after APAP treatment (**Supplementary Fig. 33**). The intense attenuation of afterglow upon APAP treatment and its increase upon NAC remediation or enzymatic inhibition confirmed the utility of SPN-thiol for longitudinal imaging of hepatotoxicity *in vivo*. The signal difference was observed within 30 min, proving that SPN-thiol detected early hepatotoxicity, even before the appearance of histological changes in drug-damaged liver tissue. Moreover, the afterglow SBRs were ~25-fold higher at all time intervals compared to NIR fluorescence (**Fig. 6e**), showing the higher sensitivity of afterglow imaging for drug-induced hepatotoxicity.

DISCUSSION

We synthesized light-emitting polymer nanoparticles and screened them for afterglow luminescence imaging applications (**Fig. 1**). The irradiation of certain PPV-based SPNs forms unstable chemical defects (dioxetane units) that can spontaneously and slowly break down to release photons that result in afterglow luminescence (**Fig. 2g**). The formation of dioxetane units within PPVs is the key step toward afterglow. Its efficiency is intrinsically determined by the substituent groups on the vinyl bonds of PPVs. Although the mechanism that governs the afterglow luminescence of PPV-based SPNs resembles chemiluminescence[39], it does not require exogenous ROS to trigger the reaction. Rather, the SPNs themselves can generate $^1O_2$ under light irradiation and subsequently induce afterglow luminescence. Such an afterglow mechanism also differs from that of rare-earth-doped inorganic nanoparticles wherein the absorbed photon energy is stored in intrinsic defect lattices rather than light-induced chemical defects[8].

In addition to temperature control, the afterglow brightness of PPV-based SPNs can be down- or upregulated by scavenging or promoting the generation of $^1O_2$ (**Fig. 2f**). This principle can fine-tune the afterglow of SPNs by simply doping with NIR-absorbing $^1O_2$ sensitizer to amplify afterglow and red-shift both the pre-irradiation and emission wavelengths into the NIR region (**Fig. 3a**). The NIR absorption of SPN-NCBS5 also makes it feasible to recharge the afterglow in deep tissue for longitudinal *in vivo* imaging.

As a result of the low background noise in the absence of concurrent light excitation, the NIR afterglow of SPN-NCBS5 permit faster and more sensitive lymph node and tumor imaging than NIR fluorescence imaging (**Fig. 5**). These imaging data clearly prove that afterglow SPNs are promising for image-guided surgical resection of sentinel lymph nodes and tumor tissues. With no need for real-time light excitation and the feasibility of imaging acquisition time as short as 0.1 s (**Supplementary Figs. 34**–**36**), SPN-based afterglow imaging can simplify the instrumentation and potentially offer markedly improved freedom for surgeons.

To the best of our knowledge, these materials have the longest emission (780 nm) and half-life (396 s) of all other existing materials; existing rare-earth-doped inorganic nanoparticles have afterglow emission maxima ranging from 610 to 716 nm and half-life times of less than 200 s (**Supplementary Table 1**)[7–10,12–17,40]. Moreover, the *in vivo* NIR afterglow intensity of subcutaneously implanted SPN-NCBS5 is 5.7×10^5 (p/s/cm^2/sr)/(μg/mL), which is more than two orders of magnitude higher than other types of afterglow nanoparticles (e.g., 5.0×10^3 (p/s/cm^2/sr)/(μg/mL) for subcutaneously implanted $ZnGa_2O_4$:Cr^{3+} nanoparticles; **Supplementary Table 1**)[10]. With such a strong NIR afterglow, the SBR for the subcutaneously implanted SPN-NCBS5 in living mice can reach 3,387 ± 39 at a concentration of 12.5 μg/mL. This is substantially higher than existing afterglow nanoparticles even when tested at higher concentrations (e.g., $ZnGa_2O_4$:Cr^{3+} nanoparticles with *in vivo* SBR of 275 at 2 mg/mL; **Supplementary Table 1**)[10] as well as for the Cerenkov luminescence imaging (SBR = 155)[4]. Because of this high SBR, afterglow SPNs permitted *in vivo* imaging of tumors after systemic administration at a much lower dosage (50 μg per mouse) than other existing afterglow agents (200 to 1,000 μg per mouse), while still offering a higher SBR. In addition, afterglow SPNs are biocompatible (**Supplementary Figs. 16**, **37** and **38**) and enzymatically biodegradable (**Supplementary Fig. 19**), showing their promise for translational research.

The structural versatility of SPNs also facilitates the development of a smart activatable afterglow probe (SPN-thiol) for drug-induced hepatotoxicity in living mice (**Fig. 6**). The NIR afterglow of a biothiol-activatable probe (SPN-thiol) can be substantially activated by the main antioxidant biothiols, such as, Cys, Hcy and GSH (**Fig. 6c**), enabling real-time imaging of drug-induced hepatotoxicity in mice at an SBR level that is 25-fold higher than NIR fluorescence imaging. Notably, SPN-thiol can detect the hepatotoxicity within 30 min of drug challenge, much shorter relative to the time required for the observation of histological changes in liver (~3 h) (**Supplementary Fig. 33**)[41]. With its ideal biodistribution, the afterglow probe could also permit real-time interrogation of the key role of biothiols in other diseases such as cancer and neuroinflammation.

In summary, we have introduced SPNs as a class of biodegradable afterglow agents for optical imaging in living mice. Due to their unique afterglow mechanism, SPNs can be developed not only as a simple accumulation agent for tissue imaging but also as a smart activatable probe to report the progression of pathological processes in real time in living animals with no need for concurrent light excitation. Due to their biocompatible and biodegradable nature, irradiation and emission both within the NIR window, and facile surface modification, afterglow SPNs have great promise as an advanced molecular imaging tool with sensitivity levels not currently achievable by NIR fluorescence.

METHODS

Methods, including statements of data availability and any associated accession codes and references, are available in the online version of the paper.

Note: Any Supplementary Information and Source Data files are available in the online version of the paper.

ACKNOWLEDGMENTS

K.P. thanks Nanyang Technological University (Start-Up grant: NTUSUG: M4081627.120) and Singapore Ministry of Education (Academic Research Fund Tier 1 RG133/15 M4011559 and Tier 2 MOE2016-T2-1-098) for financial support. H.D. thanks Singapore Ministry of Education (Academic Research Fund Tier 2 MOE2015-T2-1-112 and Tier 3 MOE2013-T3-1-002) for financial support. J.V.J. thanks NIH HL 137187 and NIH HL 117048 grants for financial support.

AUTHOR CONTRIBUTIONS

K.P. conceived and designed the study. Q.M. performed the nanoparticle synthesis and *in vitro* experiments. Q.M., C.X., X.Z. and Y. L. performed the *in vivo* experiments. K.P., Q.M., H.D., X. L. and J.V.J. contributed to the analysis and interpretation of results and preparation of the manuscript draft. K.P., Q.M., H.D., X.L., J.V.J. and all other authors contributed to the writing of this paper.

COMPETING FINANCIAL INTERESTS

The authors declare no competing financial interests.

1. Ntziachristos, V., Ripoll, J., Wang, L.V. & Weissleder, R. Looking and listening to light: the evolution of whole-body photonic imaging. *Nat. Biotechnol.* **23**, 313–320 (2005).

2. Smith, A.M., Mancini, M.C. & Nie, S. Bioimaging: second window for in vivo imaging. *Nat. Nanotechnol.* **4**, 710–711 (2009).
3. Chu, J. *et al.* A bright cyan-excitable orange fluorescent protein facilitates dual-emission microscopy and enhances bioluminescence imaging in vivo. *Nat. Biotechnol.* **34**, 760–767 (2016).
4. Thorek, D.L., Ogirala, A., Beattie, B.J. & Grimm, J. Quantitative imaging of disease signatures through radioactive decay signal conversion. *Nat. Med.* **19**, 1345–1350 (2013).
5. So, M.K., Xu, C., Loening, A.M., Gambhir, S.S. & Rao, J. Self-illuminating quantum dot conjugates for in vivo imaging. *Nat. Biotechnol.* **24**, 339–343 (2006).
6. Liu, H. *et al.* Intraoperative imaging of tumors using Cerenkov luminescence endoscopy: a feasibility experimental study. *J. Nucl. Med.* **53**, 1579–1584 (2012).
7. le Masne de Chermont, Q. *et al.* Nanoprobes with near-infrared persistent luminescence for in vivo imaging. *Proc. Natl. Acad. Sci. USA* **104**, 9266–9271 (2007).
8. Maldiney, T. *et al.* Controlling electron trap depth to enhance optical properties of persistent luminescence nanoparticles for in vivo imaging. *J. Am. Chem. Soc.* **133**, 11810–11815 (2011).
9. Maldiney, T. *et al.* The in vivo activation of persistent nanophosphors for optical imaging of vascularization, tumours and grafted cells. *Nat. Mater.* **13**, 418–426 (2014).
10. Li, Z. *et al.* Direct aqueous-phase synthesis of sub-10 nm "luminous pearls" with enhanced in vivo renewable near-infrared persistent luminescence. *J. Am. Chem. Soc.* **137**, 5304–5307 (2015).
11. Lécuyer, T. *et al.* Chemically engineered persistent luminescence nanoprobes for bioimaging. *Theranostics* **6**, 2488–2524 (2016).
12. Maldiney, T. *et al.* In vivo optical imaging with rare earth doped $Ca_2Si_5N_8$ persistent luminescence nanoparticles. *Opt. Mater. Express* **2**, 261–268 (2012).
13. Abdukayum, A., Chen, J.T., Zhao, Q. & Yan, X.P. Functional near infrared-emitting Cr^{3+}/Pr^{3+} co-doped zinc gallogermanate persistent luminescent nanoparticles with superlong afterglow for in vivo targeted bioimaging. *J. Am. Chem. Soc.* **135**, 14125–14133 (2013).
14. Liu, F. *et al.* Photostimulated near-infrared persistent luminescence as a new optical read-out from Cr^{3+}-doped $LiGa_5O_8$. *Sci. Rep.* **3**, 1554 (2013).
15. Maldiney, T. *et al.* In vivo imaging with persistent luminescence silicate-based nanoparticles. *Opt. Mater.* **35**, 1852–1858 (2013).
16. Sharma, S.K. *et al.* Persistent luminescence of $AB_2O_4:Cr^{3+}$ (A = Zn, Mg, B = Ga, Al) spinels: new biomarkers for in vivo imaging. *Opt. Mater.* **36**, 1901–1906 (2014).
17. Shi, J. *et al.* Multifunctional near infrared-emitting long-persistence luminescent nanoprobes for drug delivery and targeted tumor imaging. *Biomaterials* **37**, 260–270 (2015).
18. Toppari, J. *et al.* Male reproductive health and environmental xenoestrogens. *Environ. Health Perspect.* **104** (Suppl. 4), 741–803 (1996).
19. Maldiney, T. *et al.* In vitro targeting of avidin-expressing glioma cells with biotinylated persistent luminescence nanoparticles. *Bioconjug. Chem.* **23**, 472–478 (2012).
20. Maldiney, T. *et al.* Synthesis and functionalization of persistent luminescence nanoparticles with small molecules and evaluation of their targeting ability. *Int. J. Pharm.* **423**, 102–107 (2012).
21. Kobayashi, H. & Choyke, P.L. Target-cancer-cell-specific activatable fluorescence imaging probes: rational design and in vivo applications. *Acc. Chem. Res.* **44**, 83–90 (2011).
22. Lovell, J.F., Liu, T.W., Chen, J. & Zheng, G. Activatable photosensitizers for imaging and therapy. *Chem. Rev.* **110**, 2839–2857 (2010).
23. Chen, L.J. *et al.* Activatable multifunctional persistent luminescence nanoparticle/copper sulfide nanoprobe for in vivo luminescence imaging-guided photothermal therapy. *ACS Appl. Mater. Interfaces* **8**, 32667–32674 (2016).
24. Feng, L. *et al.* Conjugated polymer nanoparticles: preparation, properties, functionalization and biological applications. *Chem. Soc. Rev.* **42**, 6620–6633 (2013).
25. Wu, C. & Chiu, D.T. Highly fluorescent semiconducting polymer dots for biology and medicine. *Angew. Chem. Int. Ed.* **52**, 3086–3109 (2013).
26. Qian, C. *et al.* Light-activated hypoxia-responsive nanocarriers for enhanced anticancer therapy. *Adv. Mater.* **28**, 3313–3320 (2016).
27. Zhen, X. *et al.* Intraparticle energy level alignment of semiconducting polymer nanoparticles to amplify chemiluminescence for ultrasensitive in vivo imaging of reactive oxygen species. *ACS Nano* **10**, 6400–6409 (2016).
28. Pu, K. *et al.* Semiconducting polymer nanoparticles as photoacoustic molecular imaging probes in living mice. *Nat. Nanotechnol.* **9**, 233–239 (2014).
29. Hong, G. *et al.* Ultrafast fluorescence imaging in vivo with conjugated polymer fluorophores in the second near-infrared window. *Nat. Commun.* **5**, 4206 (2014).
30. Lyu, Y., Xie, C., Chechetka, S.A., Miyako, E. & Pu, K. Semiconducting polymer nanobioconjugates for targeted photothermal activation of neurons. *J. Am. Chem. Soc.* **138**, 9049–9052 (2016).
31. Ghezzi, D. *et al.* A hybrid bioorganic interface for neuronal photoactivation. *Nat. Commun.* **2**, 166 (2011).
32. Palner, M., Pu, K., Shao, S. & Rao, J. Semiconducting polymer nanoparticles with persistent near-infrared luminescence for in vivo optical imaging. *Angew. Chem. Int. Ed.* **54**, 11477–11480 (2015).
33. Scurlock, R.D., Wang, B.J., Ogilby, P.R., Sheats, J.R. & Clough, R.L. Singlet oxygen as a reactive intermediate in the photodegradation of an electroluminescent polymer. *J. Am. Chem. Soc.* **117**, 10194–10202 (1995).
34. Kim, S. *et al.* Near-infrared fluorescent type II quantum dots for sentinel lymph node mapping. *Nat. Biotechnol.* **22**, 93–97 (2004).
35. Nasr, A., Lauterio, T.J. & Davis, M.W. Unapproved drugs in the United States and the Food and Drug Administration. *Adv. Ther.* **28**, 842–856 (2011).
36. Kola, I. & Landis, J. Can the pharmaceutical industry reduce attrition rates? *Nat. Rev. Drug Discov.* **3**, 711–716 (2004).
37. Willmann, J.K., van Bruggen, N., Dinkelborg, L.M. & Gambhir, S.S. Molecular imaging in drug development. *Nat. Rev. Drug Discov.* **7**, 591–607 (2008).
38. Pessayre, D., Mansouri, A., Berson, A. & Fromenty, B. Mitochondrial involvement in drug-induced liver injury. *Handb. Exp. Pharmacol.* 311–365 (2010).
39. Dodeigne, C., Thunus, L. & Lejeune, R. Chemiluminescence as diagnostic tool. A review. *Talanta* **51**, 415–439 (2000).
40. Maldiney, T. *et al.* Effect of core diameter, surface coating, and PEG chain length on the biodistribution of persistent luminescence nanoparticles in mice. *ACS Nano* **5**, 854–862 (2011).
41. Shuhendler, A.J., Pu, K., Cui, L., Uetrecht, J.P. & Rao, J. Real-time imaging of oxidative and nitrosative stress in the liver of live animals for drug-toxicity testing. *Nat. Biotechnol.* **32**, 373–380 (2014).

ONLINE METHODS

Chemicals. All chemicals were purchased from Sigma-Aldrich unless otherwise stated. Poly(2,5-dioctyl-1,4-phenylenevinylene) (POPPV), poly[(9,9′-dioctylfluorenyl-2,7-diyl)-alt(benzo[2,1,3]thiadiazol-4,7-diyl)] (PFBT), poly(5-(2-ethylhexyloxy)-2-methoxycyanoterephthalylidene) (MEHCPV), poly[2-methoxy-5-(2-ethylhexyloxy)-1,4-phenylene] end-capped with dimethylphenyl (MEHPP) and poly[2,5-bisoctyloxy]-1,4-phenylenevinylene] (BOPPV) were purchased from Luminescence Technology Corp. Dodecaethylene glycol octadecyl ether amine (C_{18}-PEG_{12}-NH_2, PEG M_W 528) was purchased from Creative PEGWorks (Winston Salem, NC). Water was supplied by Milli-Q Plus System (Millipore Corporation, Breford, USA).

Materials characterization. TEM images were obtained on a JEM 1400 TEM with an accelerating voltage of 100 kV. Dynamic light scattering was performed on the Malvern Zetasizer Nano S. UV-Vis spectra were recorded on a Shimadzu UV-2450 spectrophotometer. Fluorescence measurements were carried out on a Fluorolog 3-TCSPC spectrofluorometer (Horiba Jobin Yvon). ^{1}H NMR and ^{13}C NMR spectra were recorded on a Bruker Advance II 300 and 75 MHz NMR, respectively. FT-IR was performed on Nicolet 8700 FT-IR Spectrometer. White light was obtained from a LED Fiber Optic Illuminator with a 150 W light bulb. This was used to irradiate samples. The distance from source to sample was 2.5 cm (irradiation spot size of 3.14 cm^2) at a power density of 0.1 W/cm^2. The 514-nm laser excitation (1 W/cm^2) used a green light laser (Stellar-Pro ML/150, Modu-Laser, Centerville, UT, United States) with a 514-nm filter. An 808-nm high-power NIR Lasers (operating mode: CW, output power after fiber: 2.5 W, LED display: diode current, multimode fiber, fiber core diameter: 400 μm, fiber connector: SMA905, with tunable laser driver module: 0–100%, laser spot size: 1 cm^2) purchased from CNI Co., Ltd. was used to irradiate the samples or other irradiation sites with a distance of 2 cm (power density: 1 W/cm^2) for 1 min to generate the afterglow luminescence unless otherwise noted. ESI-MS spectra were obtained on a Thermo Finnigan Polaris Q quadrupole ion trap mass spectrometer (ThermoFisher Corporation) equipped with a standard ESI source. Fluorescence, afterglow luminescence images, fluorescence spectra and afterglow luminescence spectra of SPNs were acquired with Luminometer (Promega, USA) or IVIS Spectrum imaging system.

Synthesis of $C_{18}PEG_{12}$-DNBS. Dodecaethylene glycol octadecyl ether amine (C_{18}-PEG_{12}-NH_2, 80 mg, 0.1 mmol) and Et_3N (27.5 μL, 0.2 mmol) were dissolved in anhydrous CH_2Cl_2. The 2,4-dinitrobenzensufonyl chloride (53 mg, 0.2 mmol) was added dropwise to the above solution at 0 °C, and then the solution was stirred for 8 h at room temperature under nitrogen. After the reaction, the mixture was diluted with CH_2Cl_2 and washed with water. The organic solvent was removed under reduced pressure, and the reaction mixture was purified by column chromatography (CH_3OH/CH_2Cl_2, 1:8) to yield the pure product $C_{18}PEG_{12}$-DNBS (103 mg, 80%). Mass of $C_{18}PEG_{12}$-DNBS: calculated for $C_{48}H_{90}N_3O_{18}S$, [(M+H)$^+$]: 1028.59, obsvd. ESI/MS: 1028.18. ^{1}H NMR of $C_{18}PEG_{12}$-DNBS (300 MHz, $CDCl_3$, **Supplementary Fig. 39**) δ (p.p.m.): 8.52 (dd, J_1 = 8.4 Hz, J_2 = 2.1 Hz,1 H), 8.35 (d, J = 8.4 Hz, 1 H), 6.66 (t, 1 H), 3.61(m, 51 H), 3.45 – 3.55 (m, 8 H), 3.42 (t, 2 H), 3.33 (m, 2 H), 1.54 (t, 2 H), 1.22 (m, 47 H), 0.84 (m, 3 H). ^{13}C NMR of $C_{18}PEG_{12}$-DNBS (75 MHz, $CDCl_3$, **Supplementary Fig. 40**) δ (p.p.m.): 149.61, 147.97, 139.80, 132.54, 126.92, 120.54, 71.56, 70.55, 70.42, 70.34, 70.04, 69.12, 43.79, 31.92, 29.69, 29.65, 29.50, 29.35, 26.09, 22.68 and 14.11.

Preparation of SPN-MEHPPV and **SPN-NCBS.** A mixed THF solution (1 mL) containing MEHPPV (0.25 mg/mL) and PEG-*b*-PPG-*b*-PEG (20 mg/mL) was used to prepare SPN-MEHPPV by rapidly injecting it into distilled-deionized water (9 mL, Milli-Q water) under continuous sonication with a microtip-equipped probe sonicator (Branson, W-150) at a power output of 6 W RMS for 2 min. For SPN-NCBS, the mixed THF solution (1 mL) contained MEHPPV (0.25 mg/mL), PEG-*b*-PPG-*b*-PEG (20 mg/mL) and NCBS (from 0 to 0.025 mg/mL, according to the doping amount). After sonication, THF was evaporated at 65 °C under nitrogen atmosphere. The aqueous solution was filtered through a polyethersulfone (PES) syringe-driven filter (0.22 μm) (Millipore), and washed three times using a 50 K centrifugal filter units (Millipore) under centrifugation at 3,500 r.p.m. for 15 min at 4 °C. The concentrations of SPN-MEHPPV or SPN-NCBS solutions were determined by UV-Vis absorption according to their absorption coefficients. The SPNs solutions were finally concentrated to 0.1 mg/mL (based on the mass of MEHPPV) by ultrafiltration and stored in dark at ~4 °C. Other SPNs, such as SPN-PFBT, SPN-MEHPP, SPN-MEHCPV, SPN-POPPV, SPN-BOPPV and SPN-MDMOPPV were prepared in a similar way. All the concentrations of SPNs were based on the mass of SP. The molar and mass extinction coefficients of SPN-MEHPPV are calculated to be 1.15×10^8 M^{-1} cm^{-1} and 85 l g^{-1} cm^{-1}, respectively. Thus, the molar mass of a nanoparticle is calculated to be 1.35×10^6 g M^{-1}. According to the molecular weight of MEHPPV, the number of MEHPPV polymers per nanoparticle is ~27.

Preparation of SPNs with different size. For preparation of SPN-PP, the procedure is similar to the preparation of SPN-MEHPPV, except that PEG-*b*-PPG-*b*-PEG (20 mg/mL) was replaced by PEG-PLGA (PP, containing PEG Mn 2,000 and PLGA Mn 4,500) (2 mg/mL). For SPN-DP, the THF-$CHCl_3$ (1:4) solution (1 mL) contained MEHPPV (0.25 mg/mL), DSPE-PEG (PEG Mn 2,000) (2 mg/mL) was used to prepare SPN-DP by rapidly injecting the above solution into distilled-deionized water (9 mL, Milli-Q water) under continuous sonication with a microtip-equipped probe sonicator (Branson, W-150) at a power output of 6 W RMS for 2 min. After sonication, organic solvents were evaporated at 65 °C under nitrogen atmosphere. The aqueous solution was filtered through a polyethersulfone (PES) syringe-driven filter (0.22 μm) (Millipore), and washed three times using a 50 K centrifugal filter units (Millipore) under centrifugation at 3,500 r.p.m. for 15 min at 4 °C. The SPNs solutions were finally concentrated to 0.1 mg/mL (based on the mass of MEHPPV) by ultrafiltration and stored in the dark at ~4 °C.

Preparation of SPN-thiol. A mixed THF solution (1 mL) containing MEHPPV (0.24 mg/mL), NCBS (12.5 μg/mL), $C_{18}PEG_{12}$-DNBS (0.5 mg/mL) and DSPE-PEG (0.125 mg/mL) was used to prepare SPN-thiol by rapidly injecting the mixture into distilled-deionized water (9 mL, Milli-Q water) under continuous sonication with a microtip-equipped probe sonicator (Branson, W-150) at a power output of 6 W RMS for 2 min. After sonication, THF was evaporated at 65 °C under nitrogen atmosphere. The aqueous solution was filtered through a polyethersulfone (PES) syringe-driven filter (0.22 μm) (Millipore), and washed three times using a 50 K centrifugal filter units (Millipore) under centrifugation at 3,500 r.p.m. for 15 min at 4 °C. The concentrations of SPN-thiol solution were determined by UV-Vis absorption according to their absorption coefficients. The SPNs solutions were finally concentrated to 0.1 mg/mL (based on the mass of MEHPPV) by ultrafiltration and stored in dark at ~4 °C.

Fluorescence and afterglow luminescence imaging. Fluorescence, afterglow luminescence imaging, fluorescence spectra and afterglow luminescence spectra were performed using an IVIS Spectrum imaging system under fluorescence and bioluminescence modes, respectively. For *in vitro* imaging of nanoparticles, fluorescence images were acquired for 0.1 s with excitation at 465 ± 10 or 430 ± 10 nm, and emission at 580 ± 10 or 780 ± 10 nm unless otherwise stated. The total intensities of the fluorescence spectra recorded by an IVIS Spectrum imaging system were obtained by integrating the area. For *in vivo* experiments, fluorescence images were acquired for 0.1 s with excitation at 465 ± 10 or 710 ± 10 nm and emission at 780 ± 10 nm. For acquisition of afterglow luminescence images, samples were pre-illuminated by 514 nm or 808 nm for 1 min at a power density of 1 W/cm^2 unless otherwise noted. *In vitro* acquisition of afterglow luminescence images used 30 s of acquisition with an open filter or a specific emission filter. *In vivo* acquisition of afterglow luminescence images used 180 s with an open filter. Note that afterglow luminescence imaging can be conducted with the acquisition time as short as 0.1 s. Fluorescence and afterglow luminescence images were analyzed by ROI analysis using the Living Image 4.0 Software.

Cell culture. HeLa cervical adenocarcinoma epithelial cells were purchased from American Type Culture Collection (ATCC). HeLa cells were cultured in DMEM (Dulbecco's Modified Eagle Medium) (GIBCO) supplemented with 10% FBS (FBS) (GIBCO). The cells were maintained in an atmosphere of 5% CO_2 and 95% humidified air at 37 °C.

doi:10.1038/nbt.3987

Cytotoxicity test. Cells were seeded in 96-well plates (1,000 cells in 100 μL per well) for 24 h, and then SPN-MEHPPV or SPN-NCBS5 (final concentration 5, 10, 20 and 30 μg/mL) were added to the cell culture medium. Cells were incubated with SPN-MEHPPV or SPN-NCBS5 or saline for 24 h followed by the addition of MTT (20 μL, 5 mg/mL) for 4 h. The media was removed, and DMSO (200 μL) was added into each well and gently shaken for 10 min at room temperature to dissolve all precipitates. The absorbance of MTT at 570 nm was measured by using a SpectraMax M5 Micro plate/Cuvette Reader. Cell viability was expressed by the ratio of the absorbance of the cells incubated with SPNs solution to that of the cells incubated with culture medium only.

***In vitro* biodegradability study of SPN-NCBS5.** For blank control group, SPN-NCBS5 (25 μg/mL) solutions were incubated at 37 °C in phosphate buffer (50 mM, pH = 7.0) containing NaCl (150 mM) without any other treatment. For MPO group, SPN-NCBS5 (25 μg/mL) solutions were treated with H_2O_2 (300 μM) and MPO (50 μg/mL) at 37 °C for 8 h in phosphate buffer (50 mM, pH = 7.0) containing NaCl (150 mM). H_2O_2 (300 μM) and MPO (50 μg/mL) were replenished another three times after every 8 h incubation due to the loss of enzyme activity. For H_2O_2 control group, SPN-NCBS5 (25 μg/mL) was treated with 300 μM H_2O_2 alone and replenished another three times after every 8-h incubation.

***In vivo* clearance of SPN-NCBS5.** All animal studies were performed in compliance with the guidelines set by the Institutional Animal Care and Use Committee (IACUC), Sing Health. 8-week-old BALB/c female nude mice (InVivos Pte. Ltd., Singapore) were used for all the *in vivo* imaging. SPN-NCBS5 (0.25 mg/mL, 0.2 mL) ($n = 3$) was systematically injected through the tail vein. Fluorescence images were acquired at $t = 0$, 2 h, 4 h, 1 d, 2 d, 4 d, 6 d, 12 d, 14 d and 18 d post-injection. Fluorescence images were captured with a 0.1 s acquisition time with excitation at 710 ± 10 nm and emission at 780 ± 10 nm using the IVIS Spectrum imaging system. The fluorescence intensities of liver were analyzed by the ROI analysis using the Living Image 4.0 Software.

Subcutaneous *in vivo* imaging. Test sizes were three mice per treatment, balancing sufficient replication of results with a reduction in mice number. All mice images were included in the analyses. Cages of the mice were randomly selected for the following treatments. For subcutaneous *in vivo* afterglow imaging, a SPN-NCBS5 nanoparticle suspension at various concentrations (50 μL, 0.03, 0.06, 0.12, 0.19, 0.25 or 12.5 μg/mL) was illuminated for 1 min with an 808-nm laser at a power density of 1 W/cm^2. This was then subcutaneously injected into the dorsal side of anaesthetized mice (2% isoflurane in oxygen). Afterglow luminescence images were captured with a 180-s acquisition time and open filters via the IVIS Spectrum imaging system. For subcutaneous *in vivo* fluorescence imaging, fluorescence images were captured for 0.1 s with excitation at 465 ± 10 nm and emission at 780 ± 10 nm using the IVIS Spectrum imaging system.

***In vitro* tissue-penetration study of NIR afterglow luminescence.** SPN-NCBS5 (50 μL, 250 μg/mL) was pre-irradiated with an 808-nm laser (1 W/cm^2) for 1 min. This was then placed under chicken tissue of varying thickness (0, 1.5, 2, 3 and 4 cm). The afterglow luminescence images were acquired for 180 s with open filter in 5 s after removal of the laser. The fluorescence images were acquired for 0.1 s at 780 nm with excitation at 710 nm. For the *in situ* pre-irradiation study, the SPN-NCBS5 solutions (50 μL, 250 μg/mL) were placed under chicken tissue of varying thickness (0, 1.5, 2.5, 3 and 3.5 cm). Light irradiation was conducted through the chicken tissue with an 808- or 514-nm laser (1 W/cm^2) for 1 min. The afterglow luminescence images were acquired for 180 s with an open filter for 5 s after removal of the laser. The fluorescence images were acquired for 0.1 s at 780 nm with excitation at 710 nm.

***In vivo* tissue-penetration study of NIR afterglow luminescence and fluorescence.** For pre-irradiation-induced afterglow, the solutions of SPN-NCBS5 (50 μL, 62.5 μg/mL) were pre-irradiated with an 808- or 514-nm laser (1 W/cm^2) for 1 min. This was then placed under the abdomen of a living mouse. The afterglow luminescence images were acquired for 180 s with an open filter for 5 s after removal of the laser. For *in situ* pre-irradiation-induced afterglow, the solutions of SPN-NCBS5 (50 μL, 250 μg/mL) were placed under the abdomen of a living mouse and then irradiated through the living mouse with 808- or 514-nm laser (1 W/cm^2) for 1 min. The afterglow luminescence images were acquired for 180 s with an open filter in 5 s after removal of the laser. The fluorescence images were acquired for 0.1 s at 780 nm with excitation at 710 or 465 nm.

Lymph node imaging. Test sizes were three mice per treatment, balancing sufficient replication of results with a reduction in mice number. All mice images were included in the analyses. Cages of mice were randomly selected for the following imaging experiments. The solutions of SPN-NCBS5 (0.25 mg/mL, 0.05 mL) were illuminated and stored at −20 °C for 1 d. The warmed SPN-NCBS5 (0.25 mg/mL, 0.05 mL) was then immediately administered to the forepaw of living mice anesthetized using 2% isoflurane in oxygen via intradermal injection. At $t = 30$ min post-injection, the afterglow luminescence and fluorescence images were collected with the IVIS Spectrum imaging system. At $t = 65$ min post-injection, the mice were illuminated for 1 min by 808-nm laser at a power density of 1 W/cm^2. The afterglow luminescence and fluorescence images were then collected at 70 min, 100 min and 130 min post-injection using the IVIS Spectrum imaging system without light illumination again. During the imaging process, the mice were warmed with a heating pad under continuous isoflurane anesthesia.

Tumor mouse model. To establish tumors in 8-week-old BALB/c mice, HeLa cells (3–5 × 10^6 cells per mouse) were suspended in DMEM supplemented medium (1 mL, 10% FBS, 1% penicillin/streptomycin antibiotics), and each mouse was injected subcutaneously on the right shoulder with 0.1 mL. Tumors were allowed to grow to a single aspect of 6~8 mm (~10–15 d) before imaging experiments.

Tumor imaging. Test sizes were three mice per treatment, balancing sufficient replication of results with a reduction in mice number. All mice images were included in the analyses. Cages of tumor-bearing mice were randomly selected for the following treatments. SPN-NCBS5 (0.25 mg/mL, 0.2 mL) ($n = 3$) was systematically injected through the tail vein. Afterglow luminescence and fluorescence images were acquired at $t = 0.5$, 1, 2, 4, 8, 12, 24, 36 and 48 h post-injection. Fluorescence images were captured with a 0.1 s acquisition time with excitation at 710 ± 10 nm and emission at 780 ± 10 nm using the IVIS Spectrum imaging system. Before acquiring afterglow luminescence images, the mice were illuminated for 1 min with an 808-nm laser at a power density of 0.5 W/cm^2 (the 808-nm high-power NIR laser was adjusted the 5.5 W output power and was used to irradiate the whole body of mouse with a distance of 15 cm). Afterglow luminescence images were captured with a 180 s acquisition time with an open filter using IVIS Spectrum imaging system.

Biodistribution method. The mice were euthanized by CO_2 asphyxiation 48 h after administration of SPN-NCBS5 (0.25 mg/mL, 0.2 mL) ($n = 3$). Major organs were collected and then placed onto black paper. All organs were pre-irradiated with an 808-nm laser (0.5 W/cm^2) for 1 min, and the afterglow luminescence images were acquired for 180 s with an open filter using IVIS Spectrum imaging system. The afterglow luminescence intensities for each individual organ were analyzed by the ROI analysis using the Living Image 4.0 Software.

***In vivo* real-time monitoring of temperature during photothermal therapy.** Nude mice with HeLa tumor xenografted were anesthetized using 2% isoflurane in oxygen ($n = 3$). SPNs (100 μL containing SPN-MEHPPV (250 μg/mL) and SPN-CPD (8 μg/mL) were locally injected into the tumor of living mice using an insulin syringe. The solution was carefully injected into the five symmetric positions of tumor (20 μL for each injection), and the injection sites were controlled to be ~0.2 cm away from the skin. Thermal images of living mouse after injection of SPNs under laser irradiation at 808 nm for 1 min at different powers of 0.4, 0.7, 1 and 1.5 W/cm^2, respectively. For acquisition of afterglow images, the tumor was irradiated by white light (0.1 W/cm^2) for 1 min together with different powers of laser irradiation (0.4, 0.7, 1 and 1.5 W/cm^2). Thermal images were acquired by a photothermal camera (FLIR T420). Afterglow luminescence images were captured with a 1-s acquisition time with an open filter using IVIS Spectrum imaging system.

***In vitro* biothiol detection.** For Cys "turn on" afterglow luminescence spectra, the SPN-thiol (12.5 μg/mL) was incubated with Cys (1 mM) in 1 × PBS (pH = 7.4) at 37 °C for 1 h. The afterglow luminescence spectra of SPN-thiol in the absence or presence of Cys were then acquired for 30 s at each collection filter from 540 ± 10 nm to 840 ± 10 nm with IVIS Spectrum imaging system. To test the selectivity, SPN-thiol (12.5 μg/mL) was treated with various amino acids or biothiols (1 mM arginine, asparagine, glutamine, glycine, histidine, leucine, lysine, methionine, proline, serine, valine, GSH, Hcy, and Cys) at 37 °C for 1 h. To correlate the afterglow luminescence or fluorescence with the concentration of Cys, SPN-thiol (1.25 μg/mL) was incubated with Cys at different concentrations (0, 20, 40, 60, 80, or 100 μM) in 1 × PBS (pH = 7.4) at 37 °C for 1 h. To test if ROS interferes biothiol-activatable afterglow luminescence, SPN-thiol (12.5 μg/mL) was treated with H_2O_2, $ONOO^-$, O_2^- or ·OH (10 μM) in 1 × PBS (pH = 7.4) at 37 °C for 1 h. Then GSH or Cys (1 mM) was added on the above-mentioned solution at 37 °C for 1 h. The afterglow luminescence images were acquired for 30 s with an open filter, and the fluorescence images were also acquired for 0.1 s at 780 ± 10 nm upon excitation at 465 nm.

***In vivo* imaging of drug-induced hepatotoxicity.** Test group sizes were three mice per treatment, balancing sufficient replication of results with a reduction in mice number. With this sample size, the large projected difference in signal with drug-induced hepatotoxicity can ensure adequate power (d = 4.2, α = 0.003, power = 0.90 using G*Power analysis). All mice images were included in the analyses. Mice were fasted for 8 h before imaging for all drug-induced hepatotoxicity imaging. Cages of mice were randomly selected for the following treatments. Mice were treated intraperitoneally (i.p.) with APAP (300 mg/kg), saline, or NAC (200 mg/kg) before APAP (300 mg/kg) treatment. After 20 min, the APAP, saline and NAC/APAP-treated nude mice were anesthetized using 2% isoflurane in oxygen, and SPN-thiol (0.25 mg/mL, 0.2 mL) was then systematically injected through the tail vein. For inhibitor studies, mice were treated i.p. with DCE (0.2 mg/kg) 2 h before APAP treatment or with 1-ABT (100 mg/kg) 12 and 24 h before APAP treatment. The fluorescence and afterglow luminescence images were collected at t = 0, 0.5, 1, 2 and 3.5 h after SPN-thiol injection. Fluorescence images were captured with a 0.1 s acquisition time, excitation at 710 ± 10 nm, and emission at 780 ± 10 nm using IVIS Spectrum imaging system. Before acquiring afterglow luminescence images, the mice were illuminated for 1 min by 808-nm laser at a power density of 1 W/cm^2. Afterglow luminescence images were captured with 180 s of acquisition time and an open filter using IVIS Spectrum imaging system. To determine the biodistribution of SPN-thiol, mice were euthanized 4 h later. The heart, lungs, liver, kidneys, and spleen were resected and placed onto black paper. All organs were pre-irradiated by 808-nm laser (1 W/cm^2) for 1 min, and the afterglow luminescence images were acquired for 180 s using IVIS Spectrum imaging system. The afterglow luminescence intensities for each individual organ were analyzed by the ROI analysis using the Living Image 4.0 Software provided by the embedded IVIS Spectrum imaging system.

Histology. The organs were fixed in 4% formalin and then embedded in paraffin before 10-μm sectioning. Histology samples were stained by hematoxylin and eosin under standard protocols. Images were acquired using a Nikon ECLIPSE 80i microscope (Nikon Instruments Inc., NY, USA).

Data analysis. The fluorescence or afterglow luminescence data were quantified with ROI analysis using Living Image 4.0 Software. Results were expressed as the mean ± s.d. unless stated otherwise. The investigators were not blinded to the treatment group of the animals before data analysis. Statistical comparisons between two groups were determined by t-test and more than three groups were determined by one-way ANOVA. For all tests, $P < 0.05$ was considered statistically significant. All statistical calculations were performed using GraphPad Prism, including assumptions of tests used (GraphPad Software Inc., CA, USA). A **Life Sciences Reporting Summary** is available.

Data availability statement. Authors confirm that all relevant data are included in the paper and/or its supplementary information files.

doi:10.1038/nbt.3987

nature research

Corresponding author(s): Kanyi Pu

☐ Initial submission ☐ Revised version ☒ Final submission

Life Sciences Reporting Summary

Nature Research wishes to improve the reproducibility of the work that we publish. This form is intended for publication with all accepted life science papers and provides structure for consistency and transparency in reporting. Every life science submission will use this form; some list items might not apply to an individual manuscript, but all fields must be completed for clarity.

For further information on the points included in this form, see Reporting Life Sciences Research. For further information on Nature Research policies, including our data availability policy, see Authors & Referees and the Editorial Policy Checklist.

Experimental design

1. Sample size

Describe how sample size was determined.

We use G*power analysis to calculate and ensure the sample sizes fulfill adequate power (p>0.8). According to the experimental data and sample size (n), P value and effect size were calculated and the power was then calculated. If it is more than 80%, demonstrating the sample size is OK.

2. Data exclusions

Describe any data exclusions.

No data were excluded.

3. Replication

Describe whether the experimental findings were reliably reproduced.

All attempts at replication were successful.

4. Randomization

Describe how samples/organisms/participants were allocated into experimental groups.

Cages of mice were randomly selected and then divided into groups for further treatment. Then the samples were allocated into groups based on different treatment conditions.

5. Blinding

Describe whether the investigators were blinded to group allocation during data collection and/or analysis.

Blinding was not relevant to our study, there were no samples from clinical research studies.

Note: all studies involving animals and/or human research participants must disclose whether blinding and randomization were used.

6. Statistical parameters

For all figures and tables that use statistical methods, confirm that the following items are present in relevant figure legends (or in the Methods section if additional space is needed).

n/a	Confirmed
☐	☒ The exact sample size (*n*) for each experimental group/condition, given as a discrete number and unit of measurement (animals, litters, cultures, etc.)
☐	☒ A description of how samples were collected, noting whether measurements were taken from distinct samples or whether the same sample was measured repeatedly
☐	☒ A statement indicating how many times each experiment was replicated
☐	☒ The statistical test(s) used and whether they are one- or two-sided (note: only common tests should be described solely by name; more complex techniques should be described in the Methods section)
☐	☒ A description of any assumptions or corrections, such as an adjustment for multiple comparisons
☐	☒ The test results (e.g. *P* values) given as exact values whenever possible and with confidence intervals noted
☐	☒ A clear description of statistics including central tendency (e.g. median, mean) and variation (e.g. standard deviation, interquartile range)
☐	☒ Clearly defined error bars

See the web collection on statistics for biologists for further resources and guidance.

Nature Biotechnology: doi:10.1038/nbt.3987

Software

Policy information about availability of computer code

7. Software

Describe the software used to analyze the data in this study.	GraphPad Prism 6

For manuscripts utilizing custom algorithms or software that are central to the paper but not yet described in the published literature, software must be made available to editors and reviewers upon request. We strongly encourage code deposition in a community repository (e.g. GitHub). *Nature Methods* guidance for providing algorithms and software for publication provides further information on this topic.

Materials and reagents

Policy information about availability of materials

8. Materials availability

Indicate whether there are restrictions on availability of unique materials or if these materials are only available for distribution by a for-profit company.	No restrictions.

9. Antibodies

Describe the antibodies used and how they were validated for use in the system under study (i.e. assay and species).	No antibodies were used in this study.

10. Eukaryotic cell lines

a. State the source of each eukaryotic cell line used.	HeLa cervical adenocarcinoma epithelial cells were purchased from American Type Culture Collection (ATCC).
b. Describe the method of cell line authentication used.	it was authenticated by the supplier using STR analysis.
c. Report whether the cell lines were tested for mycoplasma contamination.	No contamination was detected by the supplier using Hoechst DNA stain method, agar culture method, PCR-based assay.
d. If any of the cell lines used are listed in the database of commonly misidentified cell lines maintained by ICLAC, provide a scientific rationale for their use.	No commonly misidentified cell lines were used.

Animals and human research participants

Policy information about studies involving animals; when reporting animal research, follow the ARRIVE guidelines

11. Description of research animals

Provide details on animals and/or animal-derived materials used in the study.	All animal studies were performed in compliance with the guidelines set by the Institutional Animal Care and Use Committee (IACUC), Sing Health. 8-week-old BALB/c female nude mice (InVivos Pte. Ltd., Singapore) were used for all the in vivo imaging.

Policy information about studies involving human research participants

12. Description of human research participants

Describe the covariate-relevant population characteristics of the human research participants.	The study did not involve human research participants.

Nature Biotechnology: doi:10.1038/nbt.3987